AIAA SciTech Forum
6-10 January 2020, Orlando, FL
AIAA Scitech 2020 Forum

10.2514/6.2020-1766

Design, Fabrication and Testing of an Active Camber Rotor Blade Tip

Etana Ferede * and Farhan Gandhi †
Center for Mobility with Vertical Lift (MOVE)
Rensselaer Polytechnic Institute, Troy, NY, 12180, USA

This paper presents a morphing blade design for wind turbine application with flexibility in chord-wise bending while providing sufficient stiffness to carry the aerodynamic loads. The NACA64 profile is selected for the camber morphing blade demonstrator. A corrugation concept is chosen because it is relatively easy to manufacture and provides sufficient stiffness to resist deformation due to the aerodynamic loads (through the provision of effective stringers) while providing the required flexibility for chord-wise bending. A mechanical actuation mechanism is employed to achieve the desired morphing angle and increase the stiffness of the morphing airfoil section to resist aerodynamic loading. The design of a morphing blade demonstrator is presented together with the manufacturing process. Finally, an experimental study is conducted where the morphing angle is measured for increasing actuation load and compared with FE analysis showing good agreement between the experimental results and results from the finite element analysis in addition to achieving the desired morphing angle.

I. Introduction

The highly variable aerodynamic pressure [1] on Horizontal Axis Wind Turbines (HAWTS) result in heavier blades to handle the vibratory loads, increasing the Cost Of Energy (COE). The fluctuation in the aerodynamic loads is further exacerbated as the blades get longer which results in further increase of the COE. The implementation of an active aerodynamic load control on wind turbine blades results in increased energy yield or reduced blade mass, which ultimately results in reduced COE [2].

There are several methods of controlling the aerodynamic loads on wind turbine blades [3]. Among the passive methods for aerodynamic load control is the design of bend-twist coupled rotor blades [4], where the structural properties of these blades is used to passively alleviate the loads on wind turbine components. However, this method is limited in terms of bandwidth due to inertia, and non-local blade response in addition to limited vibration reduction capability (compared to active methods).

On the side of active methods for load control is the use of Individual Pitch Control (IPC) that pitches each blade individually to regulate the aerodynamic load on each blade separately [5,6] in addition to collective pitch for power regulation. However, the performance of the IPC system reduces as the blades get longer and the blade inertia reduces the effectiveness of the IPC system in reducing vibratory loads. Furthermore, fatigue concerns on pitch bearings limits the applicability of IPC for load alleviation.

An alternative to IPC system could be the use of aerodynamic control surfaces, such as mechanical flaps [7–10] or tabs [11–14]. An example of this kind of control device is an aileron on an aircraft wing, which is an hinged control surface that is actuated in order to control the local air loads. This kind of device can be installed on the outboard section of the blade where most of the aerodynamic loads are generated. Furthermore, higher actuation bandwidth is realized by this kind of control surfaces since they can be actuated much faster compared to pitching the whole blade at the root. Unfortunately, the use of such devices has the potential of increased complexity of the mechanical design, which ultimately can increase the weight of the control mechanism [15]. In addition, the gap that exists between the control surface and part of the blade section where the control surface is attached that could negatively affect the aerodynamic performance of the blade by increasing the aerodynamic drag in addition to increasing the aeroacoustics noise [16,17].

*Research scientist, Mechanical, Aerospace, and Nuclear Engineering, ferede@rpi.edu
†Redfern Chair Professor and MOVE Director, AIAA Associate Fellow, fgandhi@rpi.edu

Structural deformation to enable the desired shape change, i.e. morphing, for mitigating vibratory loads on wind turbine blade can provide an alternative to discrete mechanical devices for load control. These structural designs will not cause any discontinuity on the blade surface and as such will not suffer from an increase in aerodynamic drag or increased aeroacoustics noise due to gaps on the blades [18]. Several morphing concepts have been investigated for aerospace [19–22] application and their application to wind turbines is well summarized in a couple of review articles [23,24]. In [25], the authors presented a study of vibratory load reductions on a 5MW wind-turbine using a new morphing concept – that of a continuously conformable blade tip, where the outboard 30% span of the blade undergoes a linear variation in camber. However, [25] focused only on the performance aspects, and did not cover the implementation of the morphing concept.

The design of morphing structures needs to satisfy conflicting requirement of being sufficiently flexible so that actuation force requirements are not prohibitively large, and at the same time sufficiently stiff to carry the aerodynamic load without substantial deformation, while also minimizing mass penalty [26] to make it a viable alternative to IPC or mechanical control surface such as flaps. This paper focuses on structural design and implementation details to support the morphing concept proposed in [25]. Conventional wind turbines in general are designed to be stiff and would require substantial modification to camber. In the current study, realization of camber deformation is based on the use of a unique corrugated core that allows for easy chordwise bending of the airfoil section while satisfying other structural and aerodynamic constraints. The morphing structure is further coupled to a linkage-based actuation mechanism. A morphing blade demonstrator is presented that considers static aerodynamic load during the design process, together with the manufacturing and testing of the demonstrator.

II. Camber morphing blade concept

A span-wise variation of camber is proposed over the outer 30% of the blade that blends seamlessly to the non-morphing part of the rotor blade, as shown in Figure 1a. Looking at Figure 1a, linear camber variation along the blade span is proposed with the maximum morphing angle realized at the blade tip. The chord-wise bending of the blade section is achieved by means of a corrugated core design (see Figure 1b). This design is preferred because it is relatively easy to manufacture and provides sufficient (span-wise) stiffness to resist deformation under aerodynamic loading (through the provision of effective stringers) while providing the required flexibility for chord-wise bending. The NACA64 profile is selected for the camber morphing blade demonstrator. This airfoil shape corresponds to the airfoil shape used on the outer blade section of NREL5MW reference wind turbine [27]. The trailing 10% of the blade section is rigid as shown in Figure 1b. The spar is the main load bearing structure making it the ideal location to attach the actuation servomotors and mechanical components.

III. Actuator requirements

The amplitude and frequency are determined by analyzing the actuator activity on camber morphing blade for wind condition representing normal turbulence [25]. The normal turbulence wind model is used to analyze wind turbine fatigue properties during its lifetime and hence provides a good indication on the activity of the actuator. Four ten minutes simulation (for 10 different mean wind speeds between cut-in and cut-out) is carried out using the normal turbulence model (in accordance with the IEC 61400-1 standard for wind turbine certification), in order to get a comprehensive picture of the actuator activity.

Figure 2 shows, over the course of turbine operation, both actuation amplitude and bandwidth requirements for a (linear) span-wise variation of camber at the outer 30% of blade region and the trailing 30% of chord [25]. The top plot presents three indicators for the range of the morphing angle across the wind speeds between cut-in and cut-out. The black and red curves represent the average and median of the morphing angle, while the blue curve shows the maximum angle for which 90% of the actuation activity is accounted. The average and median of the morphing angle are similar across the wind speeds, suggesting that most of the actuation activity is around the average value. The blue curve in Figure 2 shows that actuating the morphing blade section between ±10° should cover 90% of the required actuation activity for all considered wind speeds. An example on calculating the actuator activity is presented in the middle plot of Figure 2, where the probability density function is shown for the morphing angle at rated wind speed. A 90% actuator activity at rated wind speed is the area under the

morphing angle bins between zero and ten degrees. Finally, looking at the frequency response of the actuator activity at rated wind speed (bottom plot of Figure 2), the highest contribution to the actuator activity is mostly around 1P and with a much smaller peak at 2P. This suggest that an actuator with maximum speed of 0.2Hz (1P) should be sufficient to mitigate effectively most of the loads on wind turbine components across all wind speeds between cut-in and cut-out.

IV. Preliminary design

Figure 2, and additional results [25], clearly indicated that a camber deflection over 30% of the chord, extending over the outermost 30% of the blade span, varying linearly from zero to a maximum of 10 deg amplitude at the blade tip, was sufficient to significantly reduce the turbine vibrations. Of course, both the chord length as well as the span over which camber is implemented can be varied. This would, in turn, affect the magnitude of camber deflection required. Several factors can influence the selection of whether larger camber deflections are used over a smaller section of the blade, or smaller camber deflections are preferred over a larger section. These include aerodynamic performance, actuation requirements, and manufacturing considerations. Ultimately, cambering of the airfoil section must generate the required increments in lift coefficient (target Cl) that provide sufficient aerodynamic authority to reduce vibration. While doing so inevitably generates drag, it is desirable that the drag penalty not be excessive (or the airfoil still has a reasonable Cl/Cd). Camber deformation of the airfoil requires the actuator to overcome aerodynamic pitching moments over the cambering section due to pressure differential between the upper and lower surfaces of the airfoil. Since very high aerodynamic moments would lead to increased actuation requirement, the design should ideally seek to limit their magnitude (|Cmf|). Furthermore, structural stiffness and manufacturing considerations are key factors.

Figure 3 provides a representation of a cross-section of the blade with camber deformation over a section (C_{flap}) of the total chord (c). The figure also depicts the camber angle, θ, and the aerodynamic coefficients, corresponding to lift (Cl), drag (Cd), and moment over the cambered section (Cmf). The aerodynamic analysis Xfoil [28] is used to calculate the 2D aerodynamic coefficients over a range of representative operating conditions for variations in flap length (C_{flap}) and camber angle (θ).

As an example, Figure 4 shows a contour plot of normalized coefficients of lift (Cl) and lift over drag (Cl/Cd), along with magnitude of aerodynamic moment over the cambering section |Cmf|, for a range of flap lengths and morphing angles, evaluated at 4 deg angle of attack and Reynolds number of $9x10^6$. On this figure, the solid black lines are contours of constant normalized Cl. For example, if a normalized Cl of 1.4 is desired (implying that introduction of camber should increase lift coefficient by 40%) it is clear that a 15% chord flap would require 10 deg deflection, but a 50% chord flap would require around 5 deg deflection (half the requirements on actuator stroke and actuator rates). The red contours show that the normalized (Cl/Cd) would be only slightly higher for the 50% chord flap, compared to the 15% chord flap, for the same normalized Cl of 1.4. The aerodynamic moment coefficients (depicted by background color on the figure) remain relatively low for chord lengths up to 25-30% but rapidly increase thereafter for downward camber defections (positive θ values on Figure 4). However, it should be noted that the camber actuator has to overcome not only the aerodynamic moments (like any trailing-edge flap actuator), *but also structural stiffness when subjecting the airfoil to chordwise bending, during camber*. The structural stiffness generally dominates over the aerodynamic moments. With this study culminating in the fabrication of a camber morphing demonstrator, and recognizing the challenges associated with in-house prototyping of composite corrugated cores at smaller scales and miniaturization of actuation linkage mechanisms, a larger C_{flap} of 50% was selected for this study.

Parametric sweep is performed to determine the number of cells in the corrugated core and upper skin thickness that minimizes the required actuation force, keeps the strain on the upper skin low (allowing classical composite construction), and also reduces the strain on the lower skin. Furthermore, large global deformation under aerodynamic load needs to be avoided in addition to preserving the aerodynamic shape of the blade under aerodynamic pressure (prevent excessive local out-of-plane skin deformation, or skin bubbling/dimpling as described in [29]). Figure 5 shows the model used for the parametric sweep. The number of cells in the corrugated core in the figure is five but is subject to change during the parametric sweep. The model consists of the trailing half of the NACA64 airfoil with chord length of 1.4m (chord length at the tip of the NREL5MW blade)

and a span of 1m. From Figure 5, the top and bottom skins are shown respectively in green and blue while the corrugated section is shown in red. The model is clamped at the spar and the actuation force is applied as cable force as shown, where the cables are attached (on both sides of the model) between the spar and lower flanges of the corrugated core attached to the bottom skin, as shown in Figure 5. The cable force f_i^c is given by:

$$f_c^i = f_c \frac{1}{2}(1 + \cos \pi(x_i - 1)), \quad (1)$$

where x_i is the (normalized) distance between the spar and the attachment of cable i to the corrugation and f_c is the scaling for the applied cable force. The total cable force is the sum of all cable forces on each side of the model, given by:

$$F_c = \sum_{i=1}^{N} f_c^i, \quad (2)$$

where N is the number of cables on each side of the model. Distributing the cable tension using equation 1 allows for smooth camber deformation of the model during actuation.

The aerodynamic load is applied as pressure load, where Figure 6 shows the normalized pressure distribution, Cp, over the NACA64 airfoils upper and lower surface for α = 4° and the morphing angle of 10°. The pressure distribution Cp is scaled by the dynamic pressure at the rated wind speed (where the thrust load on the rotor peaks) and multiplied by a safety factor 2 before applying it to the model as pressure load.

The thickness of the corrugated core (red elements in Figure 5) is assumed twice the thickness of the top skin (green elements in Figure 5). The corrugated skin and the top skin are made of plain-woven fabrics of glass fiber with $[0^{\circ}/90^{\circ}]$ layout bonded together with epoxy resin. The mechanical properties of the woven glass fiber are E11 = E22 = 35GPa, G12 = 8.3GPa. The bottom skin (blue elements in Figure 5) is a sandwich panel, composed of a honeycomb core (assumed 30mm for large bending stiffness) and face-sheet (assumed 0.1mm) resulting in low axial stiffness and high axial strain capability while providing sufficient bending stiffness to resist local deformation (skin dimpling) under aerodynamic loading [29]. The sandwich panel is composed of a silicon rubber (E = 40MPa) face sheet attached to honeycomb core. The honeycomb core is glued to the corrugated section in such a way that results in minimum axial stiffness while providing sufficient bending stiffness to resist aerodynamic loads and buckling under downward camber. The silicon rubber is added for smooth surface to maintain the aerodynamic profile.

Structural analysis is carried out in ABAQUS for the maximum downward morphing angle of θ = 10° in-order to determine the required actuation force and the maximum strain of the bottom skin within the operational envelop of the wind turbine blade section provided with camber morphing. The parameters in the parametric sweep are the number of corrugation units and the thickness of the upper skin (the thickness of the corrugated core is held at twice the thickness of the upper skin). Convergence analysis based on strain energy is carried out under a cable force resulting in morphing angle of θ = 10°. For example, for a model with the number of units in the corrugated core set to 5, and thickness of the upper skin set to 1mm, the converged mesh has 3000 elements.

Figure 7 shows contour plot of the required total cable force (per side) to achieve a morphing angle of θ = 10°. The contour plot also shows the strain energy stored in the upper skin and the corrugated section together with the maximum compressive strain in the bottom skin under pure actuation force. Furthermore, the morphing angle including the actuation and aerodynamic load normalized by the morphing angle under pure actuation is shown by the blue contour lines in Figure 7. Figure 7 shows that the required actuation force and hence the strain energy stored in the system is more sensitive to the skin thickness than the number of corrugation units. The sensitivity of the required actuation force and stored strain energy to the skin thickness or number of corrugation units is further examined in Figures 8a and 8b, where the strain energy in the model and the cable force are plotted against the upper skin thickness (Figure 8a) and number of corrugation units (Figure 8a). Figure 8a shows that the stored strain energy and the required cable force to achieve a morphing angle of θ = 10◦ increases with increasing skin thickness. This is not the case with increasing the number of corrugation units as seen in Figure 8b where the cable force and strain energy in the system do not change significantly with increasing number of corrugation units.

The compressive strain in the bottom skin (green contour lines in Figure 7) vary slightly with increasing skin thickness (24% to 28% for upper skin thickness going from 1mm to 3mm). This is mainly due to improper

distribution of cable force along the chord. This is further elaborated using Figure 9a, where the strain on the bottom skin is shown for a model with upper skin thickness of 1mm and number of corrugation units set to five. Looking at Figure 9a, the lower skin close to the spar experiences more (compressive) strain than the skin close to the trailing edge. A lower and improved distribution of the compressive strain over the bottom skin is achieved by applying different distribution of cable force along the corrugated section as shown in Figure 9b (which produces the same 10° camber as the baseline). Figure 7 also shows that the morphing blade section is sensitive to the aerodynamic pressure, in that the morphing angle is reduced from the target angle of $\theta = 10°$ when the aerodynamic load is considered (blue contour line in Figure 7). To clarify this, Figures 10a and 10b show camber deformation of the blade section under aerodynamic loading for different thickness of the upper skin and corrugated section. The morphing angle under aerodynamic loading is 1.1° (upward deflection) for an upper skin thickness of 1mm (see Figure 10a). In Figure 10b, the global stiffness of the blade section is increased using thicker skins, which reduces the morphing angle to 0.4°; however, this comes at the cost of increased cable force. A different actuation mechanism (other than cables) could introduce additional stiffness (while allowing the use of the thinner skin) to the morphing blade section to resist deformation under aerodynamic loading. This is further examined in the next section.

V. Final design

The aim of the preliminary design is to determine the required number of corrugation units and skin thickness that achieves the required morphing angle of the airfoil section while considering the material allowables and actuation force requirements. For the final design, the maximum chord length of airfoil section is scaled down to 75% of the tip chord of the NREL 5MW blade due to constraints on easily available fabrication capabilities. The general prototype dimensions are 52.5cm in chord direction and 91cm in span direction. The fixed-section of the blade (see Figure 2a) is not part of the prototype. Figure 13 shows a 3D CAD model of the morphing blade section. Mechanical actuation is utilized to deform the blade section, where the linear motion of the actuator results in camber deformation of the airfoil section through the mechanical linkages shown in Figure 13. The main spar and all mechanical linkages are made of Aluminum 7075 ($E = 72GPa$, $\sigma_{yield} = 503MPa$, $\rho = 2.710kg/m^3$), with the thickness of all linkages of the actuation mechanism set to 10mm.

Looking at Figure 7, the lowest number of corrugation units is desired for ease of manufacturing and attachment to the actuation mechanism. Therefore, the number of corrugation units is set to five. Furthermore, the upper skin thickness that results in the lowest required cable force is 1mm. However, this design does not provide sufficient global stiffness of the morphing section to resist aerodynamic loading (assuming camber deformation under aerodynamic loading restricted to $\theta = \pm 0.5°$). An additional stiffness is provided to the morphing section by the actuation mechanism where instead of cables, linkage mechanism is chosen for both camber deformation and additional stiffness to resist aerodynamic loads. The structural design of the morphing blade section is shown in Figure 11, where the corrugated core section is 2mm thick, while the skin on the suction side is 1mm thick. The outer ten percent of the trailing edge (Tail-section in Figure 11) is a sandwich structure with foam core and 4mm glass fiber face-sheet. The black circles in Figure 11 denote connection points between the actuation mechanism and the corrugated core section. The three connection points between the actuation mechanism and the corrugated core section together with the fact that the corrugation units are not of equal width are in order to accommodate a good alignment between the morphing section and the actuation mechanism (result of an iterative design between the morphing section and the actuation mechanism). The lower skin needs to fulfil additional requirements in that it should have low membrane stiffness to accommodate large compressive strains while having high bending stiffness to resist local out-of-plane deformation under aerodynamic pressure shown in Figure 6. The design of the lower skin is not included in the present analysis and will be considered separately.

Figure 12 shows the actuation mechanism used to deform the morphing blade section. The actuation mechanism is designed using the CAD software 'Linkage' that allows for quick design and kinematic analysis of mechanical linkages [30]. The initial position of the actuation mechanism is shown in light gray while the deformed position is shown in green. The point P_0 is fixed but is allowed to rotate while the point P_1 is constrained to move only vertically under an applied load (red arrow) and is also allowed to rotate. An iterative design of the linkage mechanism is carried out such that the vertical motion of P_1 is translated by the linkage mechanism into an arch movement of the connection points between the actuation mechanism and the corrugated section (P_2 to P_4),

shown as black arrows in Figure 12. This mode of deformation does not stretch the upper skin and the corrugated core and hence reduces the required amount of force to camber the morphing section. Furthermore, the design of the actuation mechanism is such that it provides additional stiffness to the morphing blade section when the mechanism is locked in place.

Figure 14 shows the finite element model of the morphing blade section. The finite element model consists of 3000 quadrilateral reduced integration (S4R) elements. The actuation mechanism on each side of the model consists of 3791 quadrilateral reduced integration (S4R) elements resulting in total 10582 elements for modeling the morphing section together with the actuation mechanism. Static non-linear analysis is performed where a vertical load is applied at two linkage points (see Figure 14) that deforms the morphing blade section to achieve a morphing angle of 10°.

Figure 15a and 15b show respectively the maximum in-plane principal strain in the top skin and the corrugated core. The strains in the top skin and corrugated core are the highest in chord-wise direction since the morphing blade section is designed to be flexible in chord-wise bending and stiff in the span direction. The corrugated core of the morphing section essentially acts as stringers along the blade span providing the stiffness along the blade axis. The predominant strain in the top skin (Figure 15a) is in tension with the maximum strain around 0.23%, which is less than the failure strain of glass fiber laminates (0.95%) in tension. The low in-plane strain in the top skin is expected since the design of the morphing blade section is such that most of the deformation of the top skin is in bending so that the skin is not stretched. The strain in the corrugated core (Figure 15b) is predominantly in tension (same as for the top skin), with the maximum strain of 0.28%, which is less than the failure strain of glass fiber laminates in tension. The corrugated core that goes between the top and bottom surface of the blade is flexible in chord-wise bending such that large deformation is realized without stretching the top skin or the corrugated core. The in-plane strains in the top skin and corrugated core are due to curvature change (caused by bending loads) combined with skin thickness resulting in small in-plane strains. Furthermore, the same location for maximum in-plane strain is observed for both the top skin and corrugated core, suggesting that the maximum bending in the structure is concentrated at the location shown in Figures 15a and b.

Figure 16a shows the von Mises stress on the actuation linkages. The maximum Von Mises stress is 117MPa, which is less than the yield strength of Aluminum-7075 (503MPa). The required actuation force for a camber deformation of $\theta = 10°$ is 450N per side for a 0.9m span section, less than the required cable force to deform an airfoil section (of similar size) to the same morphing angle (See Figure 7). Finally, aerodynamic load is applied to the structure while locking the actuation mechanism in place in order to check if the stiffness of the morphing structure together with the actuation mechanism is sufficient to resist deformation under aerodynamic loading. The dynamic pressure is calculated at rated wind speed of the NREL5MW machine. Figure 16b shows the deformation of the blade section under aerodynamic loading, where the resulting morphing angle is 0.1° demonstrating that the actuation mechanism adds sufficient stiffness to the airfoil section to resist camber deformation under aerodynamic load.

VI. Fabrication of a demonstrator

Figure 17 shows the production process of the morphing airfoil section. Manufacturing of the prototype is divided in two phases. For the first phase, the morphing blade section is manufactured. First, a mold is cut out of a prototyping foam with a density of $10 lb/ft^3$. A high-density foam is used to ensure a stiff mold that does not deform during the vacuum bagging process associated with the manufacturing of composite parts. Twenty shapes of the corrugated section are cut out of 2-inch thick foams using a Computer Numerical Control (CNC) machine and connected together using nine alignment rods to create a mold of 40-inch spanwise length as shown in Figure 17a. Wax release is applied on the mold and coated with PVA forming a plastic layer when dried such that the composite part releases easily from the mold when it has finished curing. Two layers of glass fiber woven mat are placed on the mold and impregnated with epoxy resin with fiber to resin ratio close to the optimum 50%. Any excess resin is removed for optimum performance. A peel ply and breather are applied over the mold. The mold is then placed in a vacuum bag and vacuum is drawn using a vacuum pump. The part is left to cure for two days at room temperature. After the curing process is completed, the corrugated part is de-molded. The top skin is manufactured following the same procedure, except the mold in this case is a stiff flat sheet. The top skin and corrugated section are then bonded together using epoxy resin and the edges are trimmed. Figure 17b shows the

top skin attached to the corrugated core.

For the second phase of manufacturing, the mechanical linkages for actuation and parts that attach the actuator and the morphing section of Figure 17b to the main spar (as shown in Figure 13) are fabricated separately. Figure 17c shows the spar with the two linear actuators and mechanical linkages that convert the direction of force exerted by the actuator (shown by green arrow) and rotates it by 90◦ in order to actuate the mechanical linkages that (camber) deform the airfoil section (shown by red arrow). Looking at Figure 17c, two actuators are placed to independently move the linkage mechanisms at either ends of the morphing section (along the span). These can be operated simultaneously or differentially to simulate a deformation mode similar to flaps or radially varying linear camber deformation. The actuation force and the stroke required to deform the morphing blade section to an equivalent flap angle of 10° is equal to 500N ≈ 112lb and 30mm ≈ 1.2in., respectively. Assuming a sinusoidal actuator motion with the desired actuation frequency of 0.2Hz, the motion of the actuator as a function of time (t) is given by $\delta = 1.2\sin(0.2 \times 2\pi \times t)$. Therefore, the maximum linear speed of the actuator is $1.2 \times 0.2 \times 2\pi \approx 1.5$in./s. Several actuators with properties close to the stated requirements are presented in Table 1. The actuator from Grainger meets all the requirements, but it is the most expensive actuator in the list. The actuator from Progressive Automations meets all the requirements except for the actuation speed and is the least expensive in the list. Given the fact that the actuation speed is not a critical factor for the demonstrator, two actuators from Progressive Automations are purchased. The actuators require a 12 volts DC power supply, where the required maximum power at the rated load of 600lb is equal to 180watt for both actuators. The morphing blade section (Figure 17b) is attached to the spar (Figure 17c), with the assembled part shown in Figure 17d. The mechanical linkage system is able to camber deform the blade section by applying a vertical motion at either end (red arrow) resulting in camber morphing of the airfoil section shown in Figure 17e.

VII. Measurement and Validation

Figure 18 shows the experiment setup where a laser pointer is attached at the tip of the camber morphing blade section and a continuous laser is projected on the white board. The board is marked with black dots that indicate the boundaries, used to determine the position of the laser point on the white board. A snapshot of the white board is taken by the camera at each deformed position of the morphing blade section to capture the position of the laser point on the white board. The engineering software MATLAB is used to analyze the resulting picture in order to determine the vertical position of the laser (δ). The morphing angle is given by:

$$\theta = \frac{180}{\pi}\frac{\delta}{l}, \qquad (4)$$

where l is the chord-wise length of the morphing blade section. There is a linear relationship between the supplied current to the actuator and the force exerted by the actuator, which is provided by the manufacturer. The maximum current supplied to the actuators is increased from 4A to 5A to successively increase the load applied. The morphing blade section is deformed three times per load level and three snapshots are taken per load level. The gray bars in Figure 20 show the morphing angle (computed using equation 4 from the vertical displacement δ) at different load levels with standard deviation per load level. The experiment shows that the prototype is capable of achieving the target morphing angle of 10° using an actuation force of 1.08 (kN).

The finite element model of the morphing blade section is also analyzed under increasing actuation load. The FE model is first modified in order to accurately represent the prototype. The FE model is extended to account for the location and direction of actuation force (to accurately model the load applied by the actuator in Figure 17c). Furthermore, the thickness of the corrugated core is modified such that it represents the additional thickness resulting from bonding the top-skin to the corrugated core (see Figure 19). Figure 20 shows in red bars the morphing angle from FE analysis for different levels of actuation force. The results from the finite element model are in good agreement with the experimental results, showing increasing morphing angle with increasing actuation force. The difference in results between the experiment and FE analysis is around 1.5% at the target angle of 10° while an average error less than 3.5% is observed over a range of 10°-16°. The small discrepancy in FEA results from the experiment shows that the morphing blade section is slightly more flexible than the FE model. This discrepancy in results between the experiment and FEA is possibly contributed to the quality of building the morphing blade section. The mechanical properties of composite parts are heavily sensitive to the manufacturing process, e.g. any voids between composite layers, misalignment of fiber angles, deviation from the optimal fiber to epoxy ratio all affect the structural properties of the composite part. This accounts mostly

for the deviation between the experimental result and the finite element analysis. However, both the experimental result and FE analysis show similar trend in the morphing angle for increasing actuation force.

Finally, the load applied by the actuator on the morphing section to achieve a morphing angle of 10° is larger than the required actuation force of 450 (N), determined in the section detailing the final design. This increase in the actuation force is due to the direction of the force applied by the actuators (Figure 17c) compared to the application of the actuator force in the final design (Figure 14). Larger force from the actuators is required since the force direction by the actuators is rotated by 90° with respect to the direction of the actuator force in Figure 14 such that only part of the actuator load results in the actuation of the mechanical linkages.

VII. Conclusions

This paper presents a camber morphing blade concept with flexibility in chord-wise bending and with sufficient stiffness to carry the aerodynamic loads. A corrugated core concept is chosen for camber morphing blade section because it is relatively easy to manufacture and provides sufficient stiffness to resist deformation under aerodynamic loading (through the provision of effective stringers) while providing the required flexibility for chord-wise bending. A parametric sweep is performed to determine the number of corrugation units and skin thickness that minimizes the required actuation force, reduces the strain on the lower skin, and prevents large global (morphing) deformation under aerodynamic load together with excessive local out-of-plane skin deformation under aerodynamic pressure that changes the aerodynamic (profile) shape of the blade section. Results from parametric analysis shows that the global stiffness of the airfoil is more sensitive to airfoil skin thickness than the number of corrugation units. However, increasing stiffness with higher skin thickness comes at the cost of increased cable force (used for airfoil camber deformation). Instead, a mechanical actuation mechanism is employed to achieve the desired camber morphing which also provides additional stiffness to the morphing blade section to resist deformation under aerodynamic loading. The design of a morphing blade demonstrator is presented together with the manufacturing process of the demonstrator. Finally, an experimental study is conducted where the morphing angle is measured for increasing actuation load and compared with FE analysis showing good agreement (within 3.5%) between the experimental results and results from the finite element analysis in addition to achieving the target morphing angle of $\theta = 10°$.

Acknowledgment

This study was funded by the New York State Energy Research and Development Authority (NYSERDA) under Award No. 58059, Continuously Conformable Wind-Turbine Blade Tip, with Mr. Gregory Pedrick and Mr. Richard Bourgeois as the Program Managers. Their support is gratefully acknowledged. NYSERDA has not reviewed the information contained herein, and the opinions expressed in this report do not necessarily reflect those of NYSERDA or the State of New York.

References

[1] Hau, E., "Wind turbines: fundamentals, technologies, application, economics", Springer Science & Business Media, 2013

[2] Berg, D. E., Wilson, D. G., Resor, B. R., Barone, M. F., Berg, J. C., Kota, S., and Ervin, G., "Active Aerodynamic Blade Load Control Impacts on Utility-Scale Wind Turbines." Tech. rep., Sandia National Lab.(SNL-NM), Albuquerque, NM (United States), 2009.

[3] Van Dam, C., Berg, D. E., and Johnson, S. J., "Active load control techniques for wind turbines." Tech. rep., Sandia National Laboratories, 2008.

[4] Bottasso, C., Campagnolo, F., Croce, A., and Tibaldi, C., "Optimization-based study of bend–twist coupled rotor blades for passive and integrated passive/active load alleviation," *Wind Energy*, Vol. 16, No. 8, 2013, pp. 1149–1166.

[5] Larsen, T. J., Madsen, H. A., and Thomsen, K., "Active load reduction using individual pitch, based on local blade flow measurements," *Wind Energy: An International Journal for Progress and Applications in Wind Power Conversion Technology*, Vol. 8, No. 1, 2005, pp. 67–80.

[6] Bossanyi, E. A., "Individual blade pitch control for load reduction," *Wind Energy: An International Journal for Progress and Applications in Wind Power Conversion Technology*, Vol. 6, No. 2, 2003, pp. 119–128.

[7] Bottasso, C. L., Croce, A., Gualdoni, F., and Montinari, P., "Load mitigation for wind turbines by a passive aeroelastic device," *Journal of Wind Engineering and Industrial Aerodynamics*, Vol. 148, 2016, pp. 57–69.

[8] Andersen, P. B., Henriksen, L., Gaunaa, M., Bak, C., and Buhl, T., "Deformable trailing edge flaps for modern megawatt wind turbine controllers using strain gauge sensors," *WindEnergy*, Vol. 13, No. 2-3, 2010, pp. 193–206.

[9] Bernhammer, L. O., van Kuik, G. A., and De Breuker, R., "Fatigue and extreme load reduction of wind turbine components using smart rotors," *Journal of Wind Engineering and IndustrialAerodynamics*, Vol. 154, 2016, pp. 84–95.

[10] Bergami, L., and Poulsen, N. K., "A smart rotor configuration with linear quadratic control of adaptive trailing edge flaps for active load alleviation," *Wind Energy*, Vol. 18, No. 4, 2015, pp. 625–641.

[11] Chow, R., and van Dam, C., "Computational investigations of deploying load control microtabs on a wind turbine airfoil," *45th AIAA Aerospace Sciences Meeting and Exhibit*, 2007, p. 1018.

[12] Baker, J., Standish, K., and van Dam, C., "Two-dimensional wind tunnel and computational investigation of a microtab modified S809 airfoil," *43rd AIAA Aerospace Sciences Meeting and Exhibit*, 2005, p. 1186.

[13] Nakafuji, D., van Dam, C., Michel, J., and Morrison, P., "Load control for wind turbines a non-traditional microtab approach, AIAA 2002-0054," *Proceedings of the 40th AIAA/ASME, Reno, NV, USA*, 2002.

[14] Yen, D., van Dam, C., Smith, R., and Collins, S., "Active load control for wind turbine blades using MEM translational tabs," *20th 2001 ASME Wind Energy Symposium*, 2001, p. 31.

[15] Daynes, S., and Weaver, P. M., "A morphing trailing edge device for a wind turbine," *Journal of Intelligent Material Systems and Structures*, Vol. 23, No. 6, 2012, pp. 691–701.

[16] Bofeng, X., Junheng, F., Qing, L., Chang, X., Zhenzhou, Z., and Yue, Y., "Aerodynamic performance analysis of a trailing-edge flap for wind turbines," *Journal of Physics: Conference Series*, Vol. 1037, IOP Publishing, 2018, p. 022020.

[17] Wilson, D. G., Berg, D. E., Barone, M. F., Berg, J. C., Resor, B. R., and Lobitz, D. W., "Active aerodynamic blade control design for load reduction on large wind turbines," *European Wind Energy Conference, Marseille, France*, Vol. 26, 2009, pp. 643–678.

[18] Daynes, S., Nall, S., Weaver, P., Potter, K., Margaris, P., and Mellor, P., "Bistable composite flap for an airfoil," *Journal of Aircraft*, Vol. 47, No. 1, 2010, pp. 334–338.

[19] Barbarino, S., Bilgen, O., Ajaj, R. M., Friswell, M. I., and Inman, D. J., "A review of morphing aircraft," *Journal of intelligent material systems and structures*, Vol. 22, No. 9, 2011, pp. 823–877.

[20] Takahashi, H., Yokozeki, T., and Hirano, Y., "Development of variable camber wing with morphing leading and trailing sections using corrugated structures," *Journal of Intelligent Material Systems and Structures*, Vol. 27, No. 20, 2016, pp. 2827–2836.

[21] DiPalma, M., and Gandhi, F., "Bi-Directional Stiffness for Airfoil Camber Morphing," *AIAA Journal*, Vol. 56, No. 4, 2017, pp. 1639–1646.

[22] Gandhi, F., Frecker, M., and Nissly, A., "Design optimization of a controllable camber rotor airfoil," *AIAA journal*, Vol. 46, No. 1, 2008, pp. 142–153.

[23] Barlas, T. K., and van Kuik, G. A., "Review of state of the art in smart rotor control research for wind turbines," *Progress in Aerospace Sciences*, Vol. 46, No. 1, 2010, pp. 1–27.

[24] Lachenal, X., Daynes, S., and Weaver, P. M., "Review of morphing concepts and materials for wind turbine blade applications," *Wind energy*, Vol. 16, No. 2, 2013, pp. 283–307.

[25] Ferede, E., and Gandhi, F., "Load Alleviation on Wind Turbines using Camber Morphing Blade Tip," *2018 Wind Energy Symposium*, 2018, p. 2020.

[26] Campanile, L., "Lightweight Shape-Adaptable Airfoils: A New Challenge for an Old Dream," *Adaptive structures: engineering applications*, 2007, pp. 89–135.

[27] Jonkman, J., Butterfield, S., Musial, W., and Scott, G., "Definition of a 5-MW reference wind turbine for offshore system development," Tech. rep., National Renewable Energy Lab.(NREL), Golden, CO (United States), 2009.

[28] Drela, M., "XFOIL: An analysis and design system for low Reynolds number airfoils," *Low Reynolds number aerodynamics*, Springer, 1989, pp. 1–12.

[29] Gandhi, F., and Anusonti-Inthra, P., "Skin Design Studies for Variable Camber Morphing Airfoils," *Smart Materials and Structures*, Vol. 17, No. 1, Feb 2008.

[30] Kim, H.-J., Jeong, Y., Kim, J.-W., and Nam, T.-J., "M. Sketch: Prototyping tool for linkage-based mechanism design," Proceedigs of the 29th Annual Symposium on User Interface Software and Technology, ACM, 2016, pp. 75-77

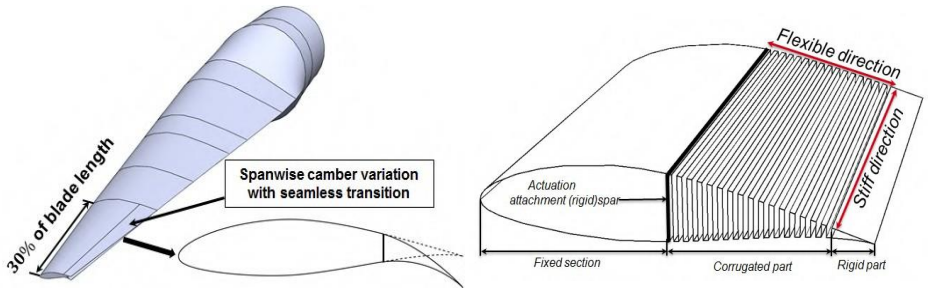

(a) Blade region with camber deformable airfoils.

(b) Structural design to achieve camber morphing.

Fig. 1 Design concept for camber morphing blade tip.

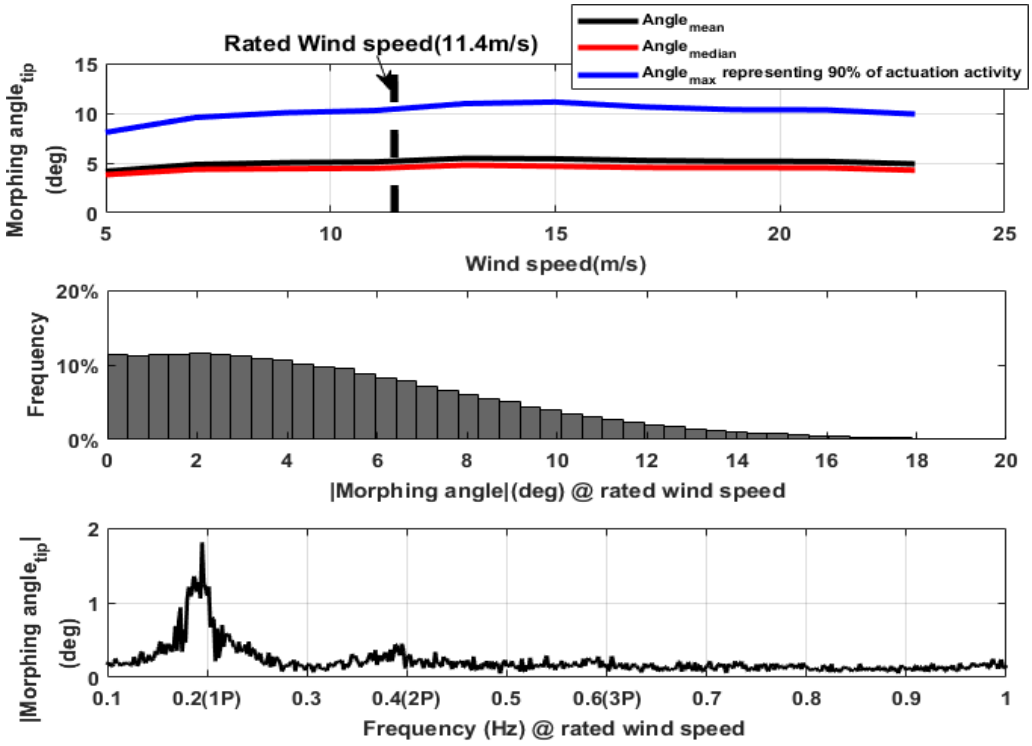

Fig. 2 Morphing actuator activity vs wind speed, probability density function and frequency response of morphing angle at rated wind speed.

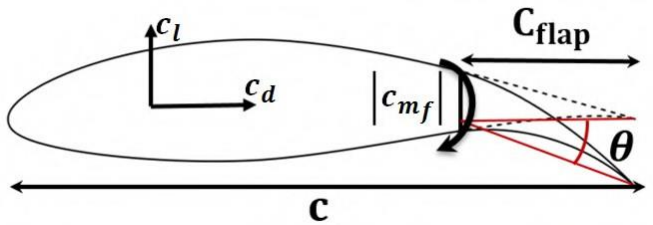

Fig. 3 Considered variables for aerodynamic performance indicators of a morphing blade section.

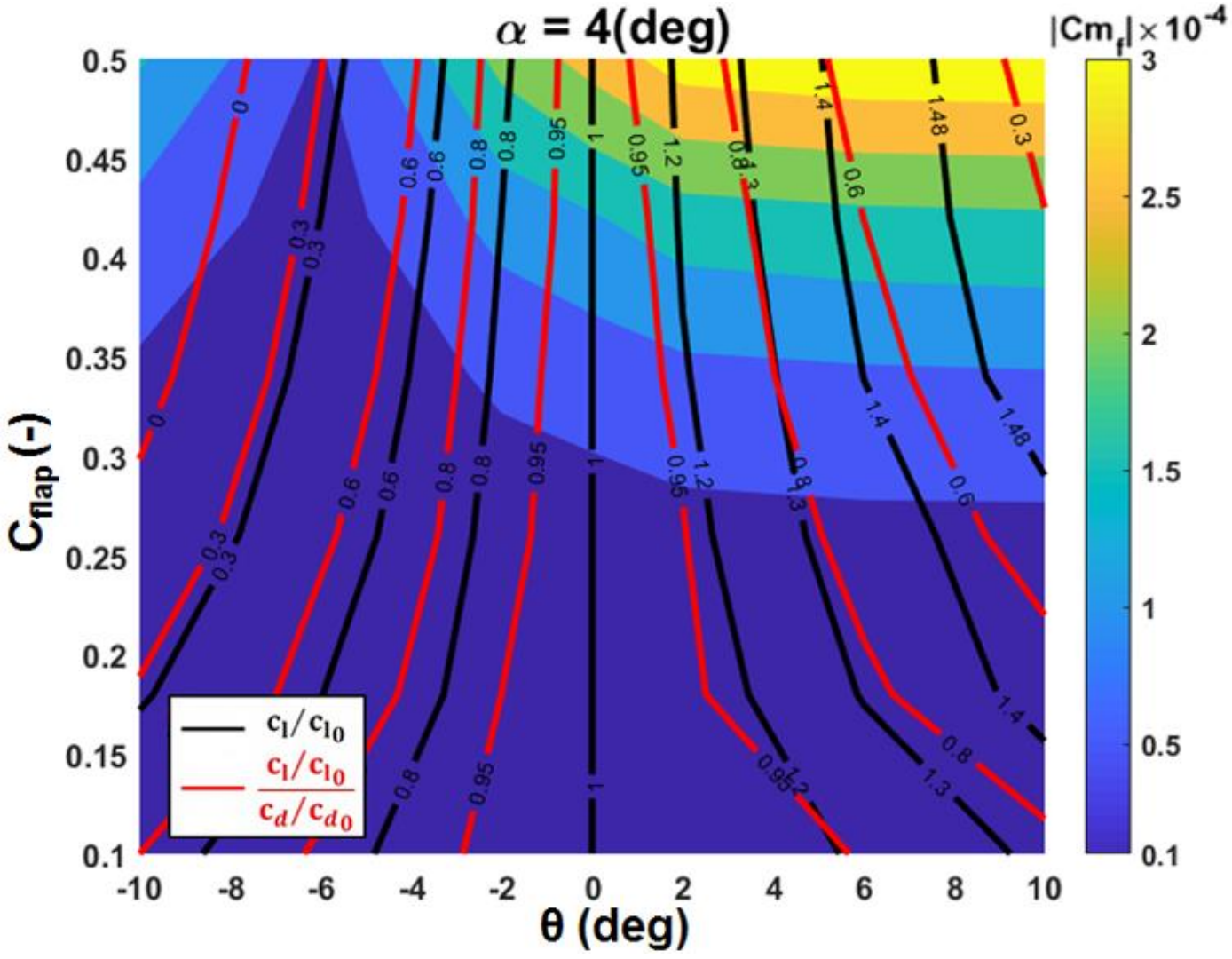

Fig. 4 Parameter sweep of the aerodynamic performance indicators.

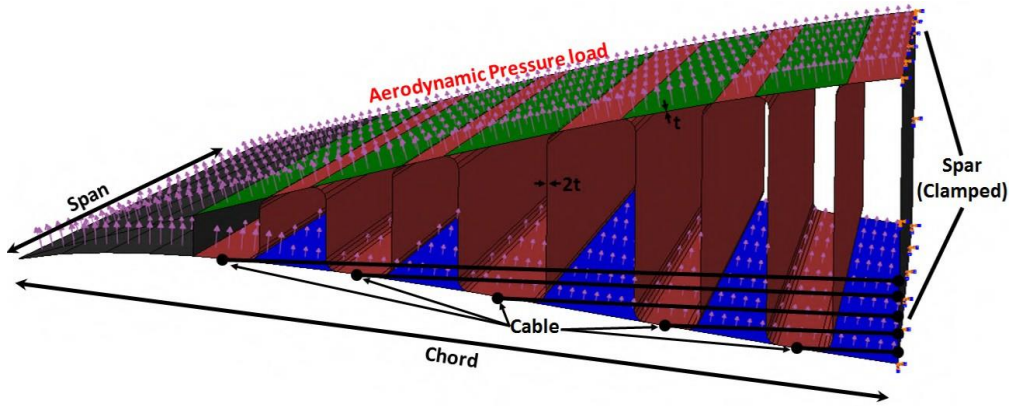

Fig. 5 Finite element model.

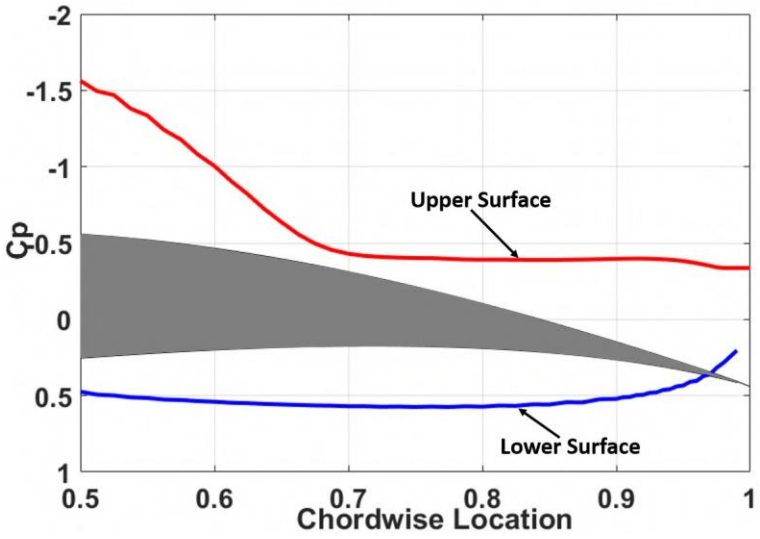

Fig. 6 Aerodynamic pressure coefficient of NACA64 (α = 4°, θ = 10°).

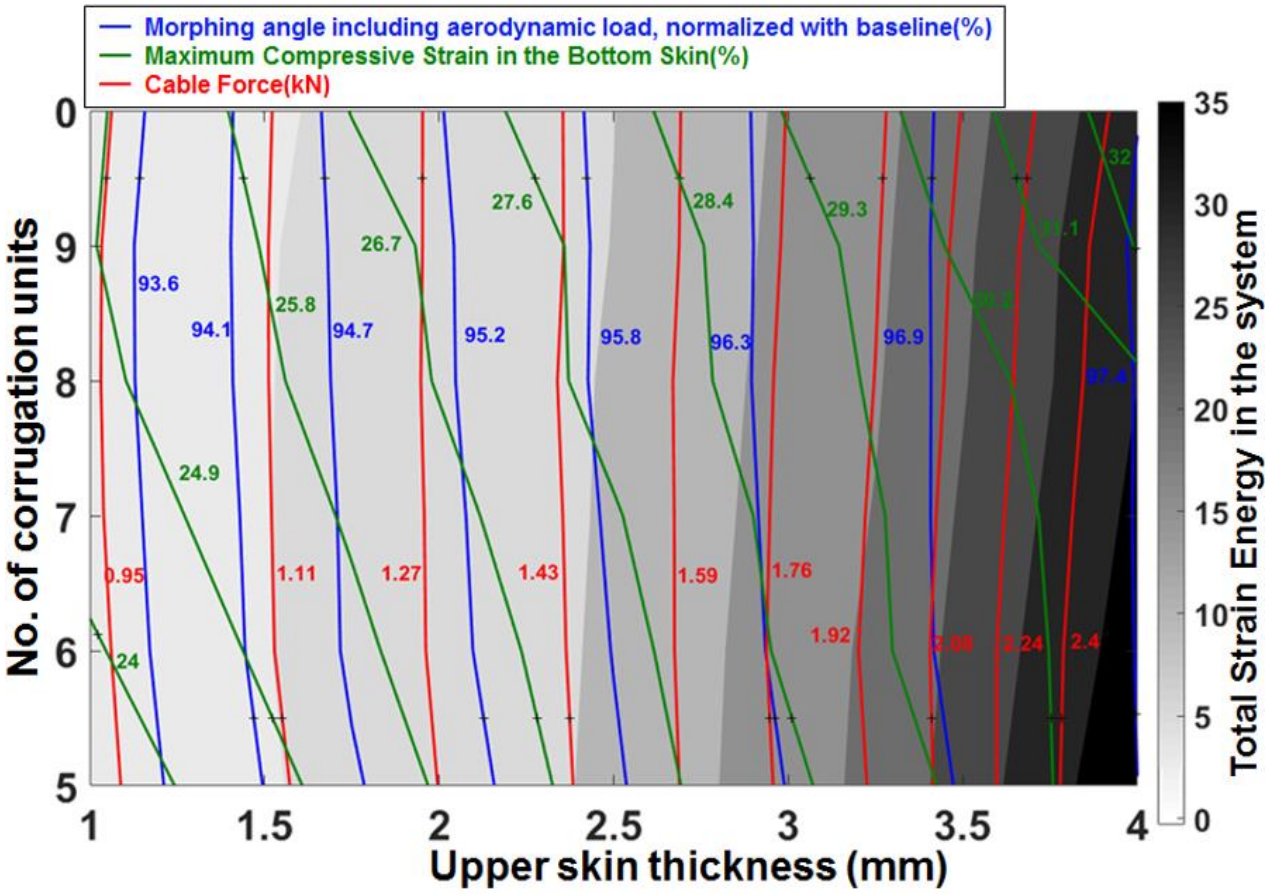

Fig. 7 Parameter sweep of the structural performance indicators.

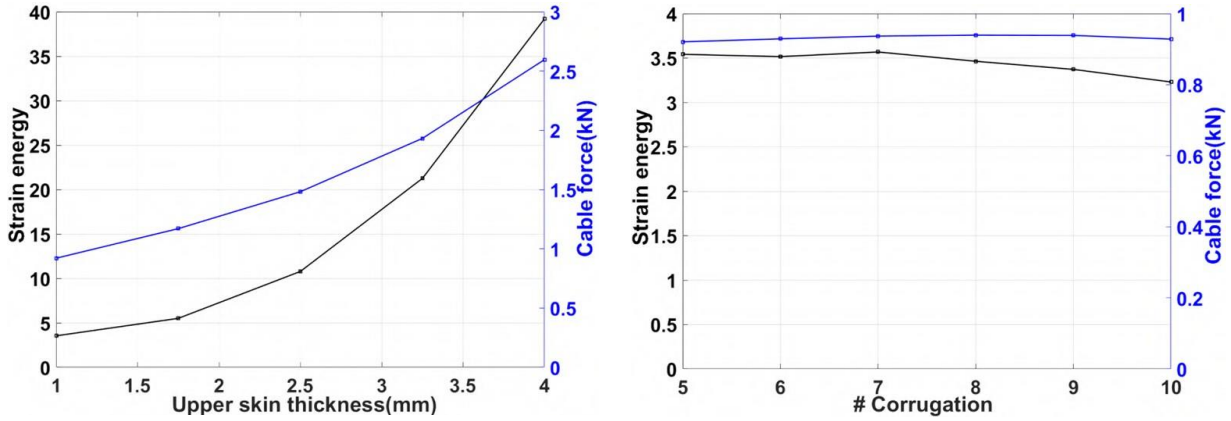

(a) for # corrugation = 5. **(b) for upper skin thickness = 1 mm.**

Fig. 8 Variation of Strain energy and cable force with respect to the skin thickness and number of corrugation.

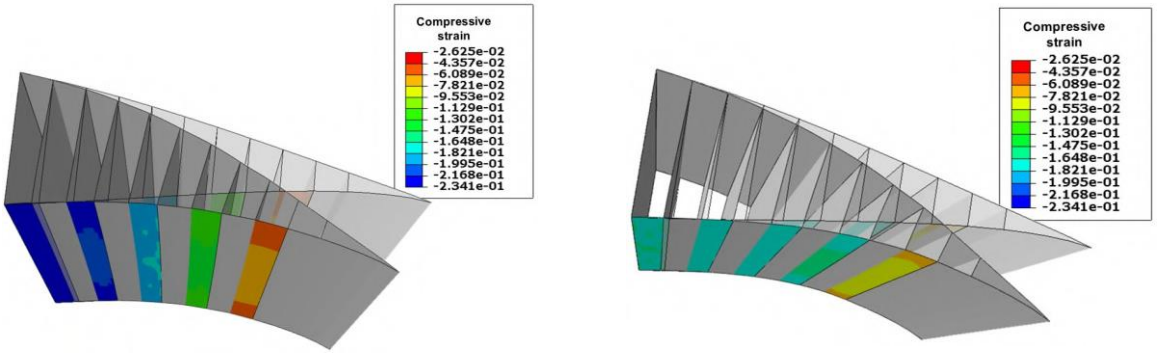

(a) Baseline cable force distribution along the chord. **(b) Improved cable force distribution along the chord.**

Fig. 9 Strain on the bottom skin for morphing angle $\theta = 10^{\circ}$.

(a) Upper skin = 1 *mm*, corrugated skin = 2 *mm*. **(b) Upper skin = 4 *mm*, corrugated skin = 8 *mm*.**

Fig. 10 Airfoil camber deformation under aerodynamic loading.

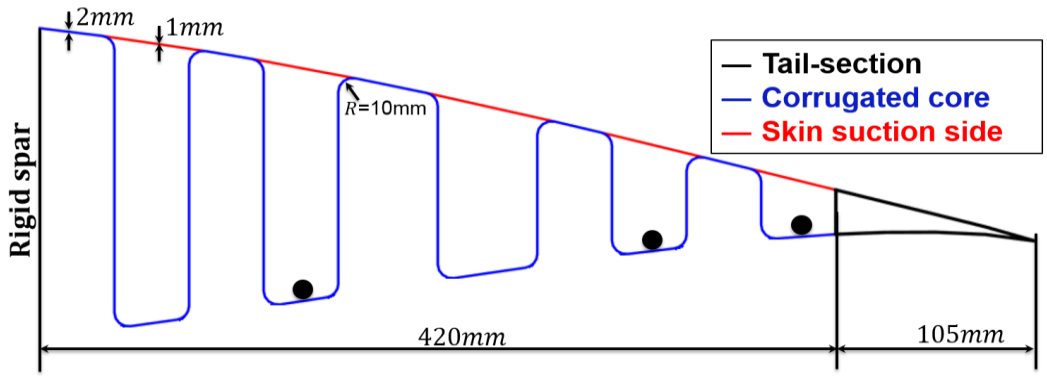

Fig. 11 Structural layout of the morphing blade section.

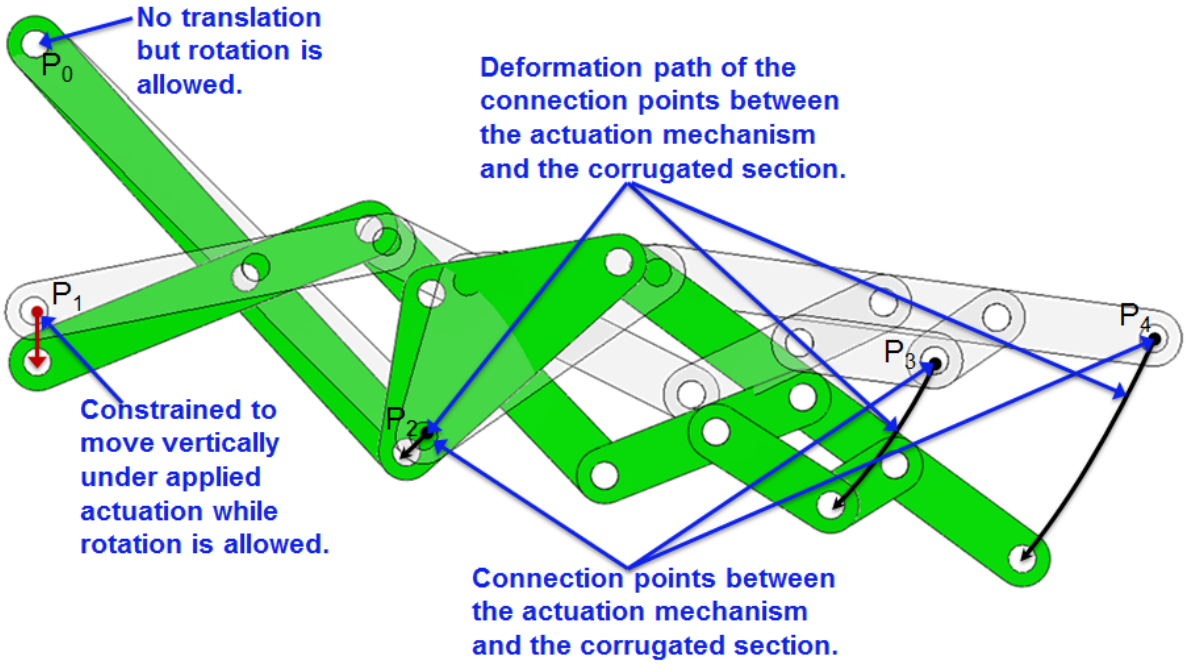

Fig. 12 Actuation mechanism.

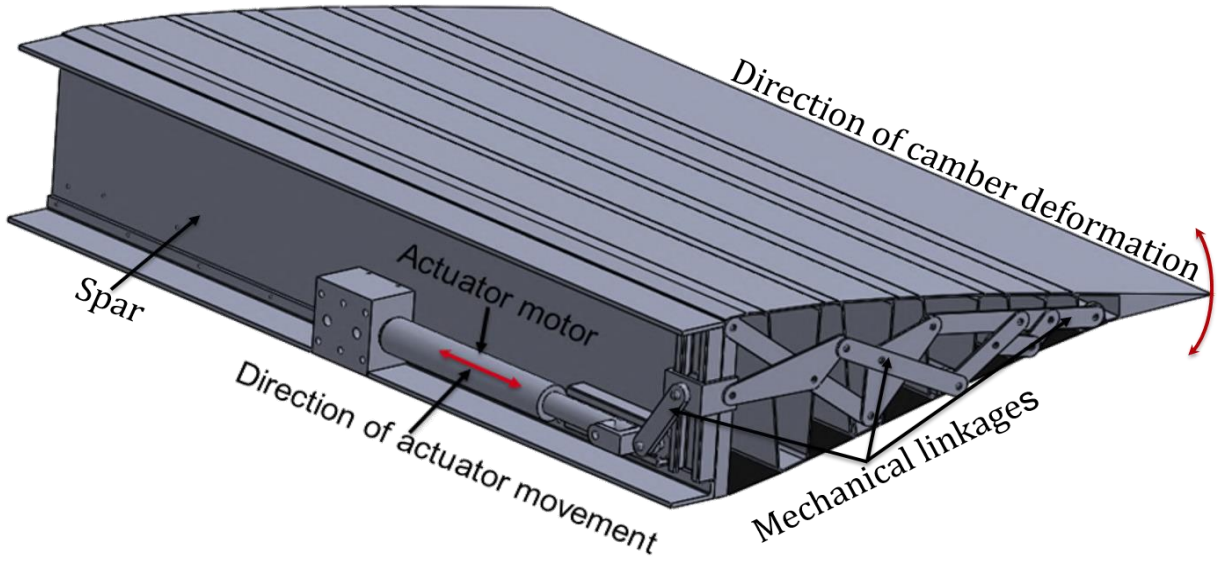

Fig. 13 CAD model of the morphing blade section with actuation mechanism.

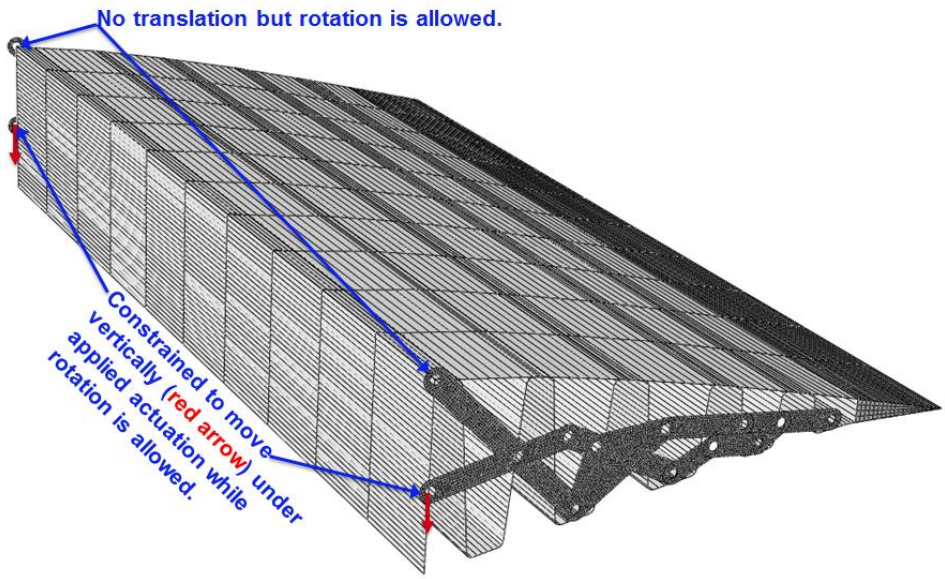

Fig. 14 Finite element model of the morphing section.

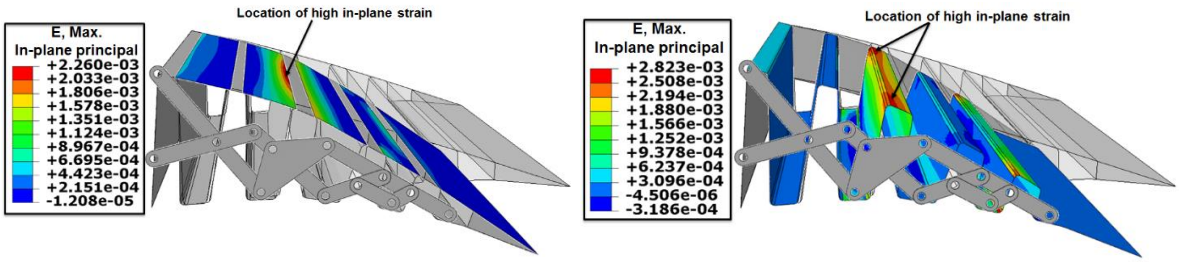

(a) Top skin. **(b) Corrugated section.**

Fig. 15 Maximum In-Plane principal strain for a camber morphing angle of $\theta = 10^{\circ}$

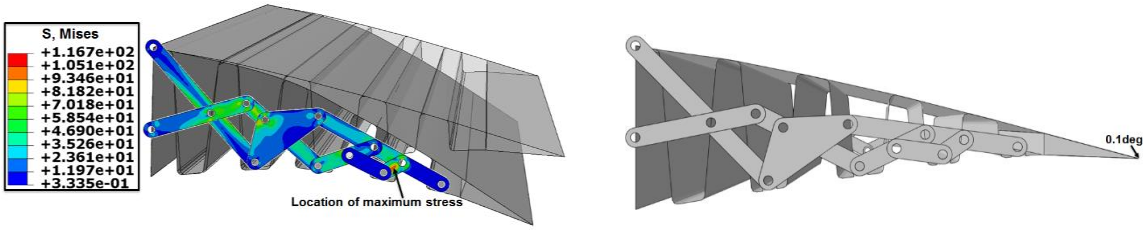

(a) Von Mises stress (MPa) of the actuation linkages for a camber loading. morphing angle of $\theta = 10^{\circ}$. **(b) Airfoil camber deformation under aerodynamic**

Fig. 16 Results of airfoil camber deformation.

Table 1 List of linear actuators.

Vendor	Cost($)	Rated load(lb)	Actuator speed at rated load(in./s)	Maximum stroke(in.)
Grainger	443	600	1	8
Progressive Automations	134	600	0.24	4
Firgelli Automations	140	400	0.3	2

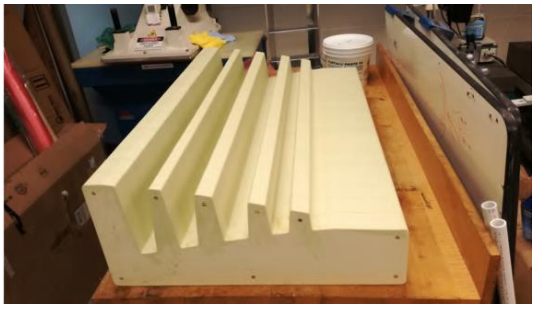

(a) Mold for the corrugated blade section.

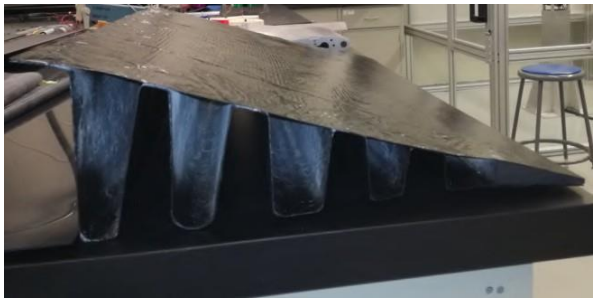

(b) Top skin bonded to the Corrugated section using epoxy.

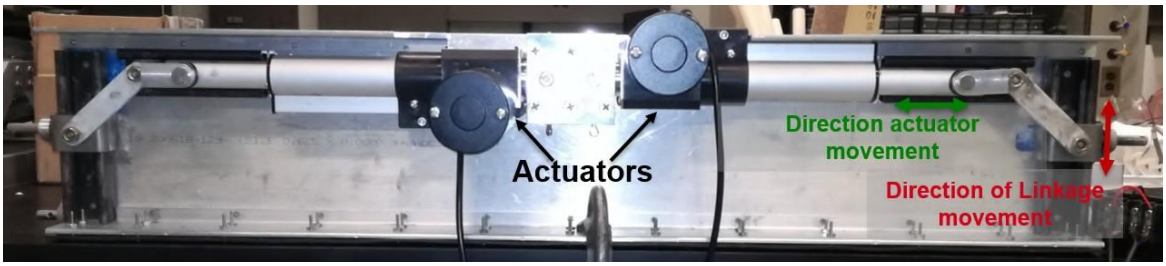

(c) Spar with actuators attached.

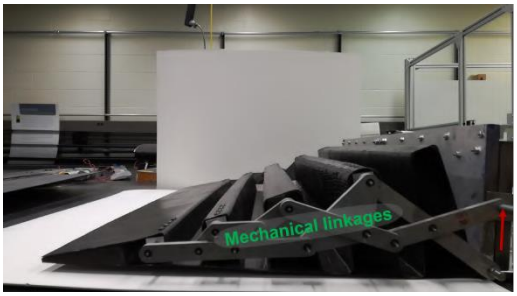

(d) Assembled morphing airfoil section, with the surface on the pressure side pointed upwards.

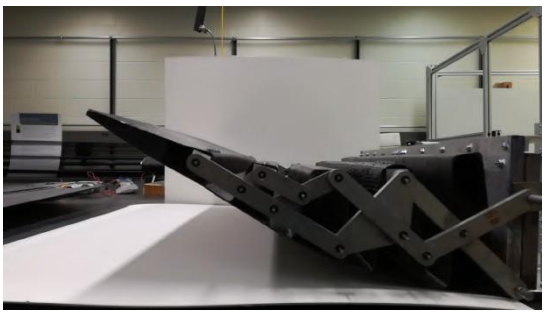

(e) Deployed blade section.

Fig. 17 Fabrication and assembly of (camber) morphing airfoil section.

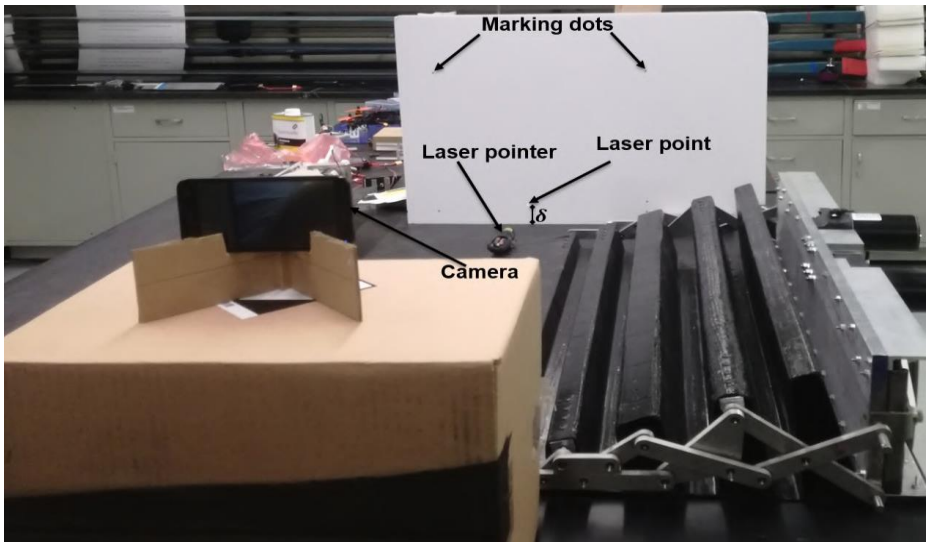

Fig. 18 Experiment Setup.

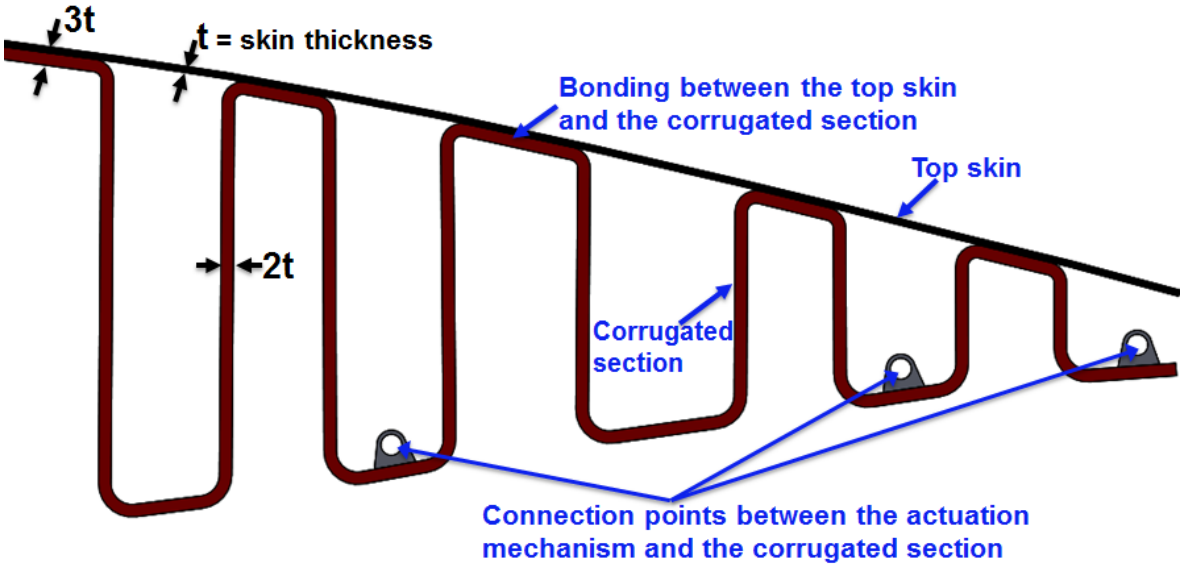

Fig. 19 Skin thickness distribution of the FE model representing the prototype.

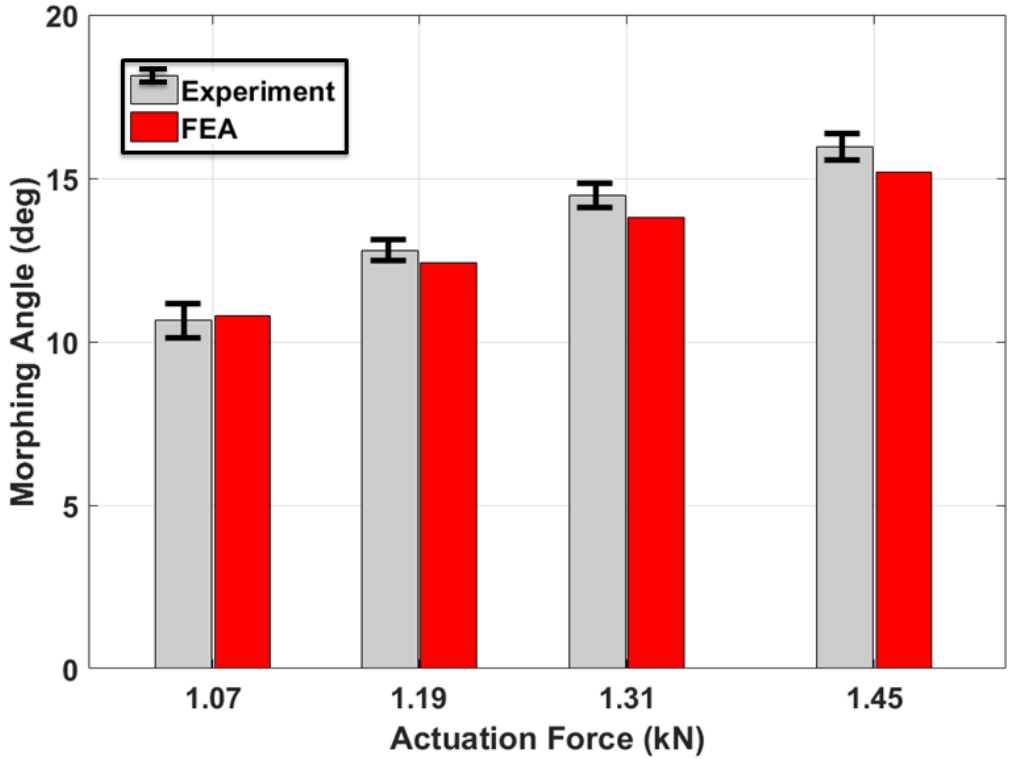

Fig. 20 Actuation force versus morphing angle.